Effect of electron correlations on the Fe_3Si and α-$FeSi_2$ band structure and optical properties

Igor Sandalov,[1,*] Natalia Zamkova,[1,2] Vyacheslav Zhandun,[1,3] Ivan Tarasov,[1,3] Sergey Varnakov,[1,3] Ivan Yakovlev,[1,3] Leonid Solovyov,[4] and Sergey Ovchinnikov[1,2,3]

[1]*Kirensky Institute of Physics, Siberian Branch of Russian Academy Sciences, 660036 Krasnoyarsk, Russia*
[2]*Siberian Federal University, Institute of Engineering Physics and Radioelectronics, 660041, Krasnoyarsk, Russia*
[3]*Siberian Aerospace University, Institute of Space Investigations and High Technologies, 660037, Krasnoyarsk, Russia*
[4]*Institute of Chemistry and Chemical Technology, Siberian Branch of Russian Academy Sciences, 660036 Krasnoyarsk, Russia*

(Received 9 June 2015; revised manuscript received 4 October 2015; published 24 November 2015)

We use the Vienna *ab initio* simulation package (VASP) for evaluation of the quasiparticle spectra and their spectral weights within Hedin's GW approximation (GWA) for Fe_3Si and α-$FeSi_2$ within the non-self-consistent one-shot approximation G_0W_0 and self-consistent scGWA with the vertex corrections in the particle-hole channel, taken in the form of two-point kernel. As input for G_0W_0, the band structure and wave functions evaluated within the generalized gradient corrected local-density approximation to density functional theory (GGA) have been used. The spectral weights of quasiparticles in these compounds deviate from unity everywhere and show nonmonotonic behavior in those parts of bands where the delocalized states contribute to their formation. The G_0W_0 and scGWA spectral weights are the same within 2%–5%. The scGWA shows a general tendency to return G_0W_0 bands to their GGA positions for the delocalized states, while in the flat bands it flattens even more. Variable angle spectroscopic ellipsometry measurements at $T = 296$ K on grown single-crystalline ∼50-nm-thick films of Fe_3Si on n-Si(111) wafer have been performed in the interval of energies $\omega \sim (1.3–5)$ eV. The comparison of G_0W_0 and scGW theory with experimental real and imaginary parts of permittivity, refractive index, extinction and absorption coefficients, reflectivity, and electron energy loss function shows that both G_0W_0 and scGW qualitatively describe experiment correctly, the position of the low-energy peaks is described better by the scGW theory, however, its detailed structure is *not* observed in the experimental curves. We suggest that the angle-resolved photoemission spectroscopy experiments, which can reveal the fine details of the quasiparticle band structure and spectral weights, could help to understand (i) if the scGWA with this type of vertex correction is sufficiently good for description of these iron silicides and, possibly, (ii) why some features of calculated permittivity are not seen in optical experiments.

DOI: 10.1103/PhysRevB.92.205129 PACS number(s): 71.20.Be, 71.20.Eh, 71.20.Gj, 75.20.Hr

I. INTRODUCTION

A hope to use the electron spin additionally to the charge as an information carrier has led to a development of the spintronics. One feasible way to exploit the spin degrees of freedom is to synthesize such magnetic semiconductors, which, on the one hand, should be magnetic at room temperature, and, on the other hand, should be easily integrated with existing semiconductor industry. Therefore, it is desirable that it should be Si based [1]. A magnetic moment can be added by transition-metal constituents. The other way is to use a magnetic metal for injecting the spin-polarized electrons into, say, Si-based semiconductor. The technologies which create magnetic epitaxial multilayer films on Si produce an interface, which contains the compounds of TSi, where T is a transition metal. This makes iron silicide compounds highly perspective materials both in bulk and film form and a detailed understanding of their physics is on demand [2]. Recently, the formation of single-crystalline Fe_3Si phases in the Fe/Si interface has been demonstrated by several groups [3–5]. The theoretical understanding of the ground-state properties like cohesive and structural properties is achieved long ago via first-principles calculations based on the various realization of local-density approximation to density functional theory [6–11].

However, the experiments, that probe the properties of materials beyond the ground state, require for their interpretation a knowledge of the single-particle *excitations*. For example, all photoeffect-based measurements belong to this class. The photoemission spectroscopy (PES) [12] provides direct measurement of the energy of electronic quasiparticles. Its extension, the angle-resolved PES (ARPES) [12], allows for extracting also perpendicular to surface momentum dependence of quasiparticle energy. Further refinement, the laser-based ARPES provides even better accuracy and resolution. A recently developed method, the time-resolved two-photon photoemission (TR-2PPE) spectroscopy [13], can monitor the state of an excited electron during the course of its transformation by laser-induced surface reaction. The transport and tunneling experiments are even more evident examples where the quasiparticle concept is a necessary ingredient for understanding the underlying physics. However, general theories sometimes are not sufficient for describing real materials. For example, the predictions of the lifetimes within the Landau theory of Fermi liquid do not describe the experiments even on Al and noble metals [14], contrary to the expectation. Indeed, electrons in these metals are well delocalized and expected to behave as a good Fermi liquid. Furthermore, TR-2PPE experiments show that the lifetime of an excited electron in Al at a fixed energy $E < E_F$ depends on the frequency of the pump pulse, i.e., on the band from which the electron originated. These examples convince that *ab initio* calculations for real materials are required. The most developed method of electronic-structure calculations, which is based on density functional theory (DFT), is designed and

*Corresponding author: sandalov@iph.krasn.ru

applicable for the ground-state properties only [14,15]. This gives rise to certain doubts that the electronic bands obtained within the framework of density functional theory (DFT) in the local- (spin-) density approximation with or without gradient corrections can be interpreted as energies of excited states. Nevertheless, the band structure, generated by the Kohn-Sham equations, is ubiquitously exploited as quasiparticle spectrum. For this reason, it makes sense to compare the quasiparticle spectrum with the Kohn-Sham bands. Here, we will compare the results of calculations within the version of gradient-corrected local-density approximation to density functional theory (GGA) and GW approximation (GWA) [14]. The name GW comes from the form of the approximation for the self-energy $\Sigma = \mathrm{G}\cdot\mathrm{W}$ in a diagram perturbation theory for electron Green's function G; W is screened by the electron-hole excitations Coulomb potential [within so-called random phase approximation (RPA)]. Both approaches have their own advantages and disadvantages. The exchange-correlation potential used in all modern implementations of the Kohn-Sham machinery contains the correlation effects that are much beyond the random phase approximation used in GWA. However, the time-independent formulations of the DFT are applicable to the description of the ground-state properties only and, besides, it is very difficult to improve the calculations by adding in a controlled way some corrections. An example of the latter is the widely used LDA + U approximation and its modifications, where many different forms of double-counting corrections are in use [16]. The nonlinear nature of DFT and an absence of a regular perturbation theory makes it difficult to perform a convincing derivation of the form of this correction. The GW method does not contain these problems; it is a well-controlled approximation. The strong advantage of GW is that it produces not only the energies of quasiparticle excitations, but also their spectral weights and lifetimes. The disadvantages of the GW approximation are that (i) it requires much more of computer resources than, say, GGA; (ii) it is applicable for description of high-density electron gas only, i.e., for $r_s \leqslant 0.5$ while in real metals $2 < r_s < 8$ (here, r_s is dimensionless interelectron distance in Bohr radius a_B units, reflecting ratio of average potential and kinetic energies); finally, (iii) the effective Hamiltonian for GW eigenvalues and eigenfunctions is not Hermitian. Both approaches are not expected to work well at high-momentum transfer, which is required for the description of the systems with d and f electrons.

Hedin's formulation of GW contains both Green's function G and the screened Coulomb potential W fully self-consistent. In practice, different levels of self-consistency and approximations are used in order to decrease the computer resources needed. The most commonly exploited is the so-called one-shot approximation $\mathrm{G_0W_0}$, with no self-consistency, where the output of GGA calculations is used as an input for it. Within the $\mathrm{G_0W_0}$, only one iteration is made, i.e., the expansion of the electron Green's function is performed with respect to the perturbation $(\Sigma - v_{\mathrm{XC}})$, where v_{XC} is the exchange-correlation potential in the GGA approach. The spectral weight of single-particle excitation with the energy E_{kn}, which is defined as [17]

$$Z_{nk} = \left(1 - \langle\psi_{nk}|\left[\frac{\partial\Sigma}{\partial\omega}\right]_{\omega=E_{nk}^{\mathrm{QP}}}|\psi_{nk}\rangle\right)^{-1}, \qquad (1)$$

in this approximation is given by the coefficient in first correction to the Kohn-Sham energy ε_{kn}:

$$E_{kn} = \varepsilon_{kn} + Z_{kn}\left[\mathrm{Re}\,\Sigma'_{\mathrm{GW}}(\varepsilon_{kn}) - \left(v_{\mathrm{XC}}^{(\mathrm{GGA})}\right)_{kn}\right]; \qquad (2)$$

the prime in Σ'_{GW} here means that it does not include the Hartree term. The absence of self-consitency makes the $\mathrm{G_0W_0}$ approximation sensitive to the input band structure, however, this is the cheapest way to calculate the excitation energies and their spectral weights which are not available within the Kohn-Sham scheme at all. Several options for self-consistency are in use, $\mathrm{G_0W}$, $\mathrm{GW_0}$, and the full one GW (see reviews [14,18]).

In $\mathrm{G_0W}$, $\mathrm{GW_0}$ approximations only eigenvalues are updating during the self-consistency procedure, but the wave functions are not updated. The self-consistent GW approximation (scGW) takes into account not only the off-diagonal components of self-energy and updates of wave functions, but includes also the vertex corrections. The situation is, however, somewhat controversial. On the one hand, the $\mathrm{G_0W_0}$ approximation often gives the results which describe PES experiments better (see, e.g., Refs. [19–21]). On the other hand, a description of the gap in semiconductors [22], as well as the ionization potentials [23], has been improved with the help of the vertex corrections to GW. Actually, a description of the local correlations (d, f electrons) also requires an improvement, namely at large momentum transfer, where the large-distance screening effects do not play a decisive role. These processes can be accounted for by the vertex corrections. Thus, the approximation to be used is material dependent and, possibly, different types of vertex corrections have to be tested for different materials. An additional motivation to include the vertex correction lies in the fact that each term in the self-consistent perturbation theory (scPT) corresponds to whole series in the non-scPT and the expansion of the self-energy within non-scPT contains in the same order the diagrams which decrease the polarization operator calculated without vertex corrections. This is seen from comparison of the corrections to the effective interaction W in the same orders of perturbation theory: an insertion of the interaction line into a fermion loop automatically decreases the number of contributing fermion loops and, therefore, generates a sign different from the sign of the graphs without such insertions. {This is especially easy to see for a single-band model by comparing two graphs, contributing to the screening of interaction in the third order: $[v(q)]^2[\Pi_0(q,E)v(q)\Pi_0(q,E)]$ and $-[v(q)]^2\Pi_1(q,E)$. Here, $\Pi_0(q,E) = \sum_k \pi(k,q,E)$ is electron-hole loop while $\Pi_1(q,E)$ is the loop with inserted interaction, $\Pi_1(q,E) = \sum_{k,p} \pi(k,q,E)v(k-p-q)\pi(p,q,E)$ where $\pi(k,q,E) = (f_k - f_{k+q})/(\epsilon_k - \epsilon_{k+q} + E)$, f_k is Fermi function. When the self-energy is calculated with these two contributions, the full compensations arise only in small phase volume of the integration due to constraints on the integration region coming from the momentum conservation, however, it may become non-negligible at large momentum transfer. As easily seen, for constant interaction, part of the graphs compensate each other exactly.} In the materials which contain in their band structure flat bands (atomiclike level), this compensation may become even more essential since the compensation of contributions in pp and ph channels may occur [see, e.g., Eq. (10) in Abrikosov's paper [24]]. A

degree of the compensation is, of course, material dependent. In particular, the detailed investigation of the influence of the ladder-type vertex corrections in the particle-hole (ph) channel on the ionization potential of the series of binary compounds has been performed in Ref. [23]. As seen from Fig. 2 of Ref. [23], although an overall agreement with the experimental ionization potential is improved, its degree is material dependent.

The situation in which both ph and pp channels of scattering are equally important is described by the parquet equations. So far, they have been studied only for models [24]. Even direct solution of the Bethe-Salpeter equations in the ph channel requires too many computer resources to be widely used for *ab initio* calculations. For this reason, the questions as to how and to which terms the vertex corrections should be applied still remain to be researched. One way to outsmart this difficulty has been suggested in Refs. [25,26]: they separated from the vertex the exchange-correlation two-point depending scattering amplitude f_{XC} from the time-dependent DFT (TDDFT) and have shown that it is sufficient for description of some spectroscopic data. This approximation sometimes is too rough. For example, the authors of [23] pointed out that it produces too large a gap for semiconductors and insulators. The authors of Ref. [28] analyzed the effect of the vertex corrections in the effective interaction W and in the self-energy Σ on the ground-state properties and excitations in the closed-shell atoms and jellium model compared to the standard GW without vertex corrections. They found that the first shows little improvement over standard GW, while for jellium the substantial improvement occurs only when the vertex is included to W, while the inclusion of it into Σ leads to unphysical results.

Here, we apply the suggestion Refs. [25,26], which was implemented [22] into VASP codes, to the *metallic* systems with *d* electrons. Following, we will compare the results of calculations for Fe_3Si and α-$FeSi_2$ within GGA, G_0W_0, and scGWA with the correction f_{XC} included and will show that for these metallic compounds the quasiparticle (QP) energy bands are described by GGA quite well, while for calculation of the spectral weights the G_0W_0 approximation is sufficient. The obtained QP band structure and spectral weights can serve as a prediction for ARPES measurements on iron silicides.

The paper is organized as follows. In Sec. II, we present the details of our *ab initio* GGA and GW calculations. The GGA and G_0W_0A densities of electron states and the band structures are compared in Sec. III; the behavior of the spectral weights of iron silicides Fe_3Si and α-$FeSi_2$ is discussed in Sec. IV. In Sec. V, we discuss the influence of self-consistency (with vertex correction) on the quasiparticle band structure. The comparison of calculated and experimentally measured optical spectra on single-crystalline Fe_3Si films grown by the molecular beam epitaxy are given in Sec. VI (particularly, the details of the experiment are given in Sec. VI A). The discussion and conclusions are given in Sec. VII.

II. CALCULATION DETAILS

The calculations presented in this paper are performed using the Vienna *ab initio* simulation package (VASP) [29] with projector augmented wave (PAW) pseudopotentials [30]. The valence electron configurations $3d^64s^2$ are taken for Fe atoms and $3s^23p^2$ for Si atoms. One part of the calculations is based on the density functional theory where the exchange-correlation functional is chosen within the Perdew-Burke-Ernzerhoff (PBE) parametrization [31] and the generalized gradient approximation (GGA). Throughout all GGA, G_0W_0, and scGW calculations, the plane-wave cutoff energy is 500 eV, and Gauss broadening with smearing 0.05 eV is used. The dielectric permittivity is calculated within the linear-response theory and random phase approximation (RPA) as implemented in VASP code [17,32]. The vertex correction to the polarizability for scGW procedure, as well as for the dielectric permittivity, is expressed approximately in terms of the exchange-correlation kernel f_{XC} [17,22,26]. The theoretical optical characteristics are calculated from the permittivity (see Figs. 13 and 14), using the formulas given in the captions to the figures.

In the GW part of calculations implemented in VASP [17], we report both G_0W_0 and scGW. The Brillouin-zone integration for G_0W_0 is performed on the grid Monkhorst-Pack [33] special points $10 \times 10 \times 10$ for Fe_3Si and $12 \times 12 \times 6$ for α-$FeSi_2$. The implemented in VASP Kramers-Kronig transformation for dielectric permeability ϵ uses a small complex shift η, which smoothes the real part of ϵ and, correspondingly, decreases the accuracy of calculations. A decrease of η requires an increase of the number of the grid points in density of states. In the present calculation, the chosen number of frequencies was 500 for G_0W_0 calculations and 336 for scGW ones. It was sufficient for working with small $\eta = 0.047$ and 0.065 eV for G_0W_0 and scGW calculations correspondingly, providing, thus, more accurate results. The GW calculations require a large number of unoccupied bands [17]. We performed calculations for 128 and 160 electronic bands. Since obtained results do not differ, we used in further calculations 128 bands.

The GGA Kohn-Sham band structure and eigenfunctions were taken as the input for the GW calculations, namely, the self-energy for G_0W_0 is computed as $\Sigma_{G_0W_0} \approx iG^{GGA}W^{GGA}$. In the scGW, the iterative procedure was carried out until the self-consistency is reached with respect to quasiparticle energies. The scGW calculations require much more computer resources; for this reason the convergence tests for this approximation for Fe_3Si were performed first at the small grid $4 \times 4 \times 4$ and 10 iterations. Then, the calculations were performed at the $8 \times 8 \times 8$ grid for Fe_3Si and at $8 \times 8 \times 4$ grid for α-$FeSi_2$. Different bands reach self-consistency with different speed; the "most difficult" happens to be the flat bands. In our calculations, seven updates provided the accuracy up to 10–40 meV, so in the following, we present the results for the seventh iteration.

Structurally these two iron silicides, Fe_3Si and α-$FeSi_2$, are quite different.

Their structures are illustrated in Fig. 1. The compound Fe_3Si belongs to DO_3 structural type with the space symmetry group $Fm\bar{3}m$. The iron atoms have two nonequivalent crystallographic positions in fcc lattice, namely, $Fe^{(1)}$and $Fe^{(2)}$ have different nearest surroundings: $Fe^{(1)}$ has eight $Fe^{(2)}$ nearest neighbors which form a cube, whereas the $Fe^{(2)}$ is in the tetrahedral surrounding of both Si and $Fe^{(1)}$ atoms.

The iron disilicides have several structural modifications. The most stable phases are α-$FeSi_2$ (right, Fig. 1) and β-$FeSi_2$

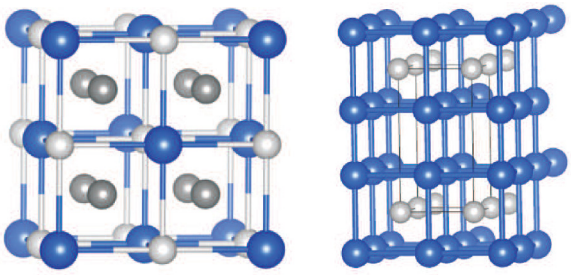

FIG. 1. (Color online) Crystal structures of Fe_3Si (left) and α-$FeSi_2$ (right). Blue balls show Si atoms. $Fe^{(1)}$ are denoted by light and $Fe^{(2)}$ by dark gray balls in Fe_3Si; light gray balls in α-$FeSi_2$ stand for Fe atoms.

phases [34,35]. The compound α-$FeSi_2$ has tetragonal lattice with $P4/mmn$ space symmetry group with one molecule per unit cell. Each iron atom here is located in the center of the cube, consisting of the silicon atoms. This structure contains the planes which are formed by only iron and by only silicon atoms. These planes are orthogonal to the tetragonal axis. Two planes formed by silicon atoms are separated by wide empty cavity, which does not contain the iron atoms.

The rhombohedral cell has been used for the Fe_3Si calculations. The equilibrium parameters and the distances between nearest Fe and Si atoms for the Fe_3Si and α-$FeSi_2$ structures have been found from the full optimization of the structure geometries within GGA and are shown in Table I. The G_0W_0 and scGW calculations have been performed with the same structural parameters.

Both spin-polarized GGA and G_0W_0 result in metallic states, ferromagnetic for Fe_3Si and paramagnetic with zero-spin Fe atoms for α-$FeSi_2$. For this reason, all further calculations for α-$FeSi_2$ have been performed within a non-spin-polarized version of VASP. The structural inequivalence of the Fe atoms' surroundings in the Fe_3Si reflects itself in both magnetic moment values and the contributions of Fe ions' d states into the electron density of states. The magnetic moment $M_{Fe^{(1)}}$ of $Fe^{(1)}$ atom is higher than the free-atom moment $M^{GGA}_{Fe^{(1)}} = 2.52\mu_B$ and $M^{GWA}_{Fe^{(1)}} = 2.55\mu_B$. The $Fe^{(2)}$ atom has much lower moment $M^{GGA}_{Fe^{(2)}} = 1.34\mu_B$ and $M^{GWA}_{Fe^{(2)}} = 1.40\mu_B$. As will be seen from the analysis of DOS, the latter moments are formed by the delocalized d states. The experimental values reported in works [36,37] are slightly different: $M^{expt}_{Fe^{(2)}} = 1.2\mu_B$, $M^{expt}_{Fe^{(1)}} = 2.4\mu_B$ in Ref. [36] and $M^{expt}_{Fe^{(2)}} = 1.35\mu_B$, $M^{expt}_{Fe^{(1)}} = 2.2\mu_B$ in Ref. [37].

TABLE I. Relaxed lattice parameters and the equilibrium distances between nearest ions. The experimental values [34] are given in brackets.

Fe_3Si	α-$FeSi_2$
$a = 5.60$ Å(5.65 Å)	$a = 2.70$ Å(2.69 Å)
$R(Fe^{(1)}\text{-}Fe^{(2)}) = 2.45$ Å	$c = 5.13$ Å(5.13 Å)
$R(Fe^{(2)}\text{-Si}) = 2.45$ Å	$z_{Si} = 0.27\,(0.28)$
$R(Fe^{(1)}\text{-Si}) = 2.83$ Å	R(Fe-Si) = 2.30 Å
	R(Si-Si) = 2.56 Å

III. COMPARISON OF GGA AND G_0W_0 DENSITIES OF ELECTRON STATES AND BAND STRUCTURE

Figure 2 displays comparison of the GGA and G_0W_0 densities of electron states (DOS) for Fe_3Si and α-$FeSi_2$. The GGA part of the results coincides with previous calculations of Fe_3Si [36,38,39] and α-$FeSi_2$ [35,38,40]. The general features of the DOS in both compounds and approximations are that the bands in the interval $[-5,+5]$ eV around Fermi energy are formed by the d electrons of iron with a slight admixture of s and p electrons of Si and Fe. The Si valent s and p electrons are delocalized in the wide energy region with smeared maximum around -4 eV in both compounds. G_0W_0 changes the intensities of the peaks mainly in the energy region deeply under Fermi surface, but the changes in Fe_3Si and α-$FeSi_2$ are different. If in the GGA DOS of the Fe_3Si the peak located at $E \sim -3.5$ eV is shifted by G_0W_0 for about 0.5 eV and made sharper, the GGA peaks in α-$FeSi_2$ DOS in approximately the same energy region (I, II in left panel of Fig. 2) are washed out within the G_0W_0 calculations.

Different chemical surroundings of the Fe atom positions, the cubic one for $Fe^{(1)}$ by $Fe^{(2)}$ atoms and the tetrahedral one for the $Fe^{(2)}$ atoms by the $Fe^{(1)}$ and Si atoms as nearest neighbors reflect themselves in different behavior of partial d-electron DOS. It is illustrated in Fig. 3.

As seen from Figs. 3(a) and 3(b), the contribution to the magnetic moment on $Fe^{(1)}$ from E_g orbitals [positive DOS in Fig. 3(a)] compensated by the contribution from T_{2g} orbitals [the negative middle peak in Fig. 3(b)]. This means that the T_{2g} orbitals are responsible for formation of the large quasilocal magnetic moment at $Fe^{(1)}$ atoms. It is also interesting that the usual splitting of the d shell into T_{2g} and E_g symmetries is violated here by the contribution from exchange interaction: as seen from Figs. 3(a) and 3(b) the E_g peak is in-between two T_{2g} peaks. Contrary to that, d DOS of $Fe^{(2)}$ is spread in a wide region of energies. The d electrons of both T_{2g} and E_g symmetries contribute to formation of magnetic moment of $Fe^{(2)}$. The delocalization of $Fe^{(2)}$ d electrons reflects itself in the smaller moment than the one on $Fe^{(1)}$. Thus, the magnetism in Fe_3Si has mixed localized-delocalized nature.

The d DOS of iron in α-$FeSi_2$, where Fe atoms also have Si atoms as neighbors, displays behavior similar to $Fe^{(2)}$ partial DOS for d electrons in Fe_3Si. However, only these delocalized electrons are not able to form magnetism in α-$FeSi_2$. The absence of magnetism in α-$FeSi_2$ is easy to understand on the basis of well-known Stoner's model for a magnetism of the delocalized electrons: the criterion $Jg(\varepsilon_F) > 1$ is not fulfilled since the density of electron states $g(\varepsilon_F)$ at the Fermi energy ε_F is too small (here J is exchange integral between delocalized electrons). An alternative mechanism of the magnetism suppression would be a formation of the low-spin state within the localized d-electron picture. This state could be formed if the crystal-field splitting of the d shell was stronger than the Hund-exchange one. However, the density of d-electron states does not contain bright peaks which might be interpreted as former d levels split in the crystal field. Thus, one can conclude that if GGA and G_0W_0 are good approximations for α-$FeSi_2$, the key mechanism of the magnetism destruction in this compound is the delocalization of d electrons.

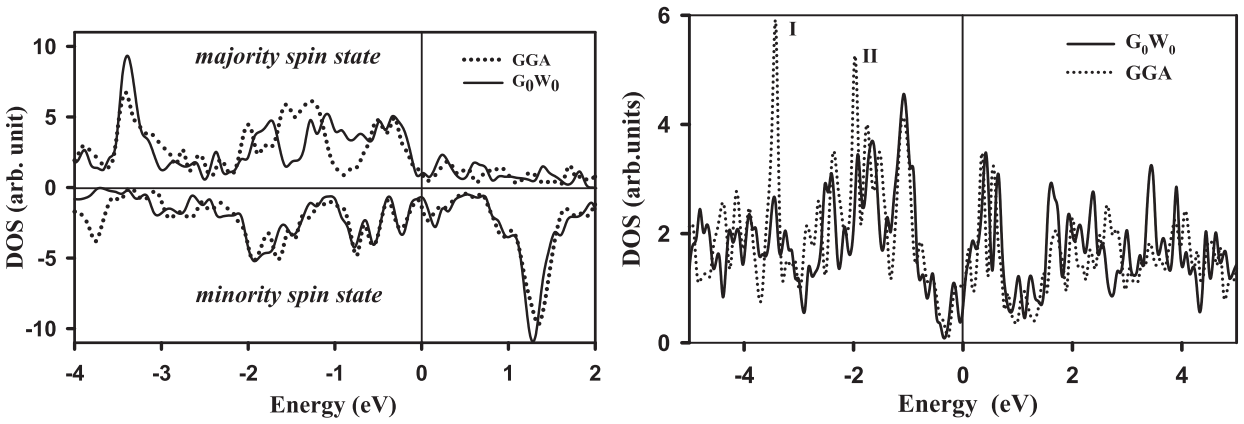

FIG. 2. Left panel: The spin-polarized density of electron states for Fe_3Si in the interval of energies $[-4,+2]$ eV. Since the GGA and the G_0W_0 approximations produce different Fermi energies $\varepsilon_F^{GGA}(Fe_3Si) = 7.88$ eV and $\varepsilon_F^{GW}(Fe_3Si) = 8.44$ eV, the plots are aligned for comparison by placing the zero in the energy axis of both plots at Fermi energy. Right panel: The DOS for α-$FeSi_2$ in the energy interval $[-5,5]$ eV with the same type of alignment of the energy axes: $\varepsilon_F^{GGA}(\alpha\text{-}FeSi_2) = 9.34$ eV and $\varepsilon_F^{GW}(\alpha\text{-}FeSi_2) = 10.03$ eV.

The most pronounced changes in G_0W_0 compared to GGA are experienced by T_{2g} electrons. It is illustrated on Fig. 4 for α-$FeSi_2$: two peaks (I and II) seen in the GGA DOS which are washed out in the G_0W_0 are formed by T_{2g} electrons. The same is valid for the "down"-spin T_{2g} states in the vicinity of the Fermi level in Fe_3Si [Fig. 3(d)]. At the same time, the well-expressed localized peaks formed by E_g orbitals remain intact.

We report here the results of the comparison only for the part of the GGA and G_0W_0 band structures which are within

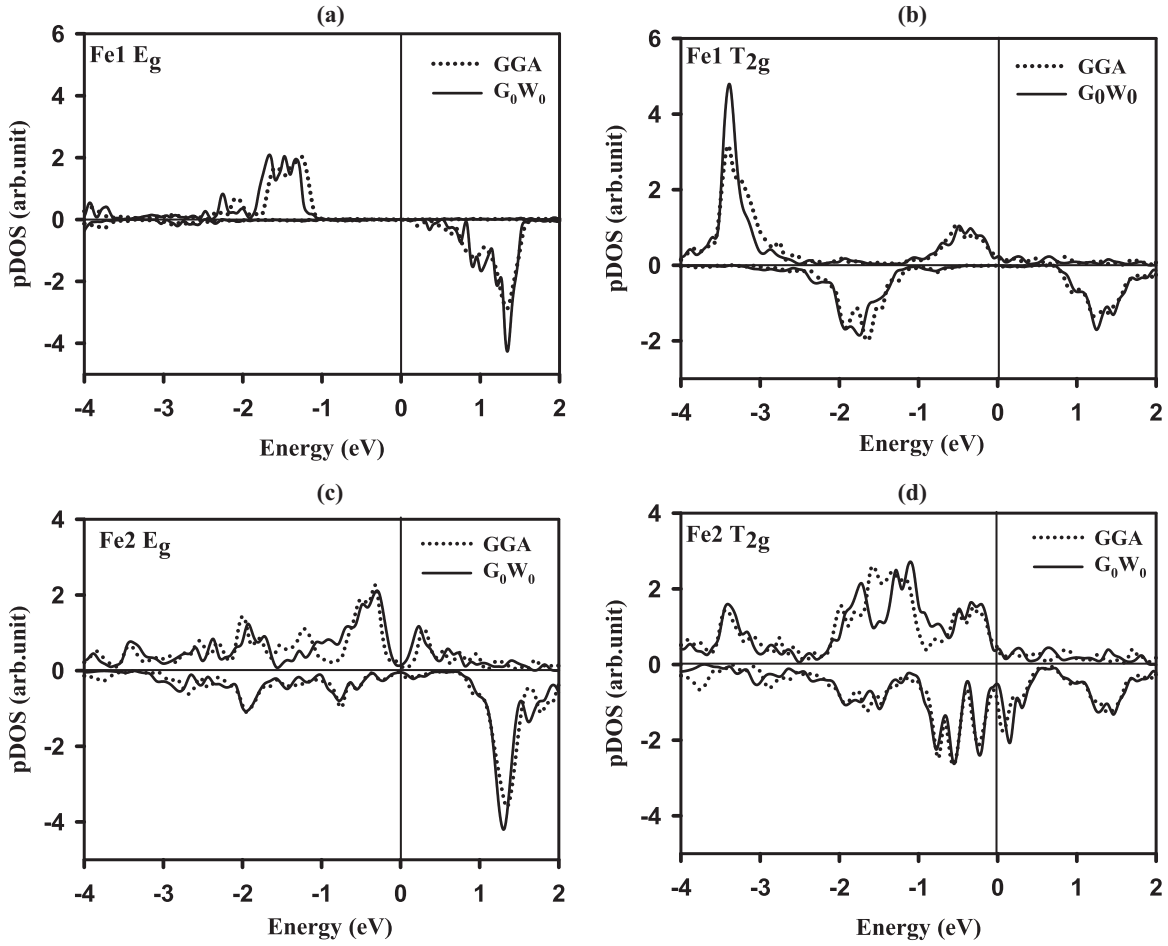

FIG. 3. The partial spin-polarized d-electron DOS for Fe_3Si . Left panels display the contribution to DOS from d_{z^2} and $d_{x^2-y^2}$ states (E_g), while the right ones show the contribution from d_{xy}, d_{xz}, and d_{yz} states (T_{2g}).

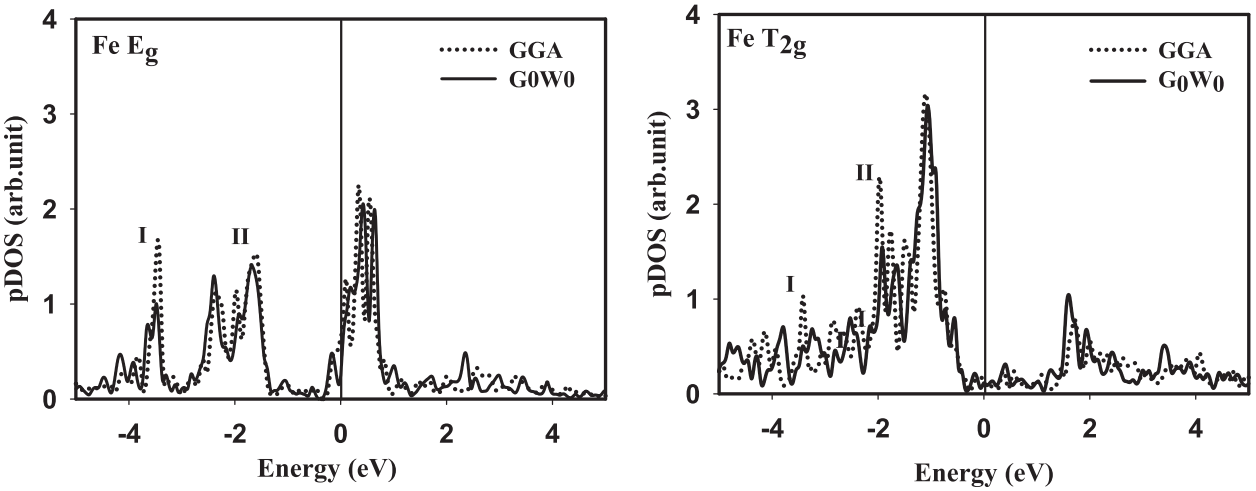

FIG. 4. The partial spin-polarized d-electron DOS α-$FeSi_2$. Left panel displays the contribution to DOS from d_{z^2} and $d_{x^2-y^2}$ states (E_g), while the right one shows the contribution from d_{xy}, d_{xz}, and d_{yz} states (T_{2g}).

several electron volts vicinity of the Fermi energies (remind that GGA and G_0W_0 generate different Fermi energies, see the caption to Fig. 2).

The Kohn-Sham band structure calculated within GGA does not differ from the known results for Fe_3Si [36,39] and for α-$FeSi_2$ [35,40,41]. Figures 5 and 6 show the band structure for Fe_3Si in the directions ΓX and ΓL, and for α-$FeSi_2$ in the directions ΓX, ΓM, and ΓZ, where $\Gamma = (0,0,0)$, $X = (2\pi/a)(1,0,0)$, $L = (\pi/a)(1,1,1)$, $M = (2\pi/a)(1,1,0)$, $Z = (2\pi/c)(0,0,1)$.

The bands are named in accordance with their symmetries in the Γ point. The closest to the Fermi energy three filled spin-up bands for the Fe_3Si in Fig. 5 (upper panel) near the Γ point, the doublet E_g and the triplet T_{2g} are formed by the d electrons of Fe atoms. The first empty band (A_{1g}) near the Γ point is formed by the s states of both Fe and Si atoms.

The GGA and G_0W_0 band structures for α-$FeSi_2$ are shown in Fig. 6. Here, the closest to the Fermi energy filled bands formed by the d orbitals of Fe atoms near the Γ point are $B_{1g}(d_{x^2-y^2})$, A_{1g} (d_{z^2}), the doublet E_g (d_{xz},d_{yz}) and $B_{2g}(d_{xy})$. The lowest shown band (A_{2u}) is formed by the s electrons of Fe and p electrons of Si. The same tendency is seen: namely the delocalized states, in this case, s and p states, show the largest difference in GGA and G_0W_0. If the band formed by d electrons close to the Fermi energy remains almost untouched, the lowest sp band is shifted in G_0W_0 by $\sim$1 eV. The first empty band near the Γ point is formed by the s and p states of both Fe and Si atoms. In general, the GGA versus G_0W_0 shift is about one electron volt for the excited states, while the band shape remains the same. As seen at the right panel of Fig. 6 in the ΓZ direction, the purely d bands are completely flat, while the dispersion which arises near the boundaries is due

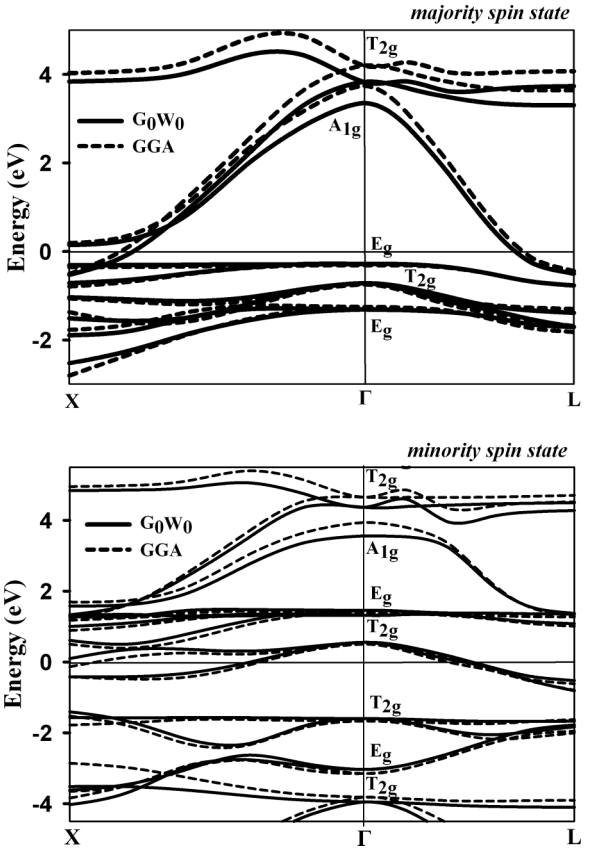

FIG. 5. The GGA and GW spin-up (top) and spin-down (bottom) bands for Fe_3Si. Zero in the energy axis of GGA and G_0W_0 plots is chosen at corresponding Fermi energies.

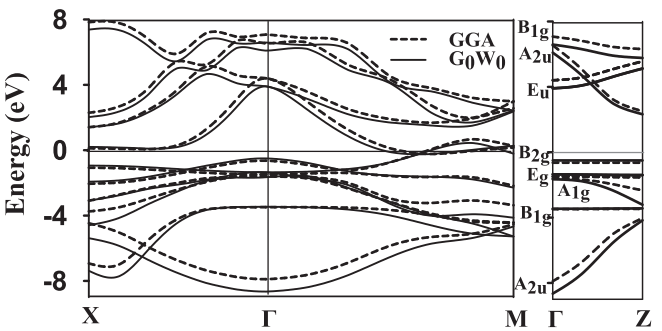

FIG. 6. The band structure of α-$FeSi_2$; zero in the energy axis of GGA and G_0W_0 plots is chosen at corresponding Fermi energies.

to the admixture of s and p states. Analogous admixture of sp electrons is observed around the boundary points X and M.

IV. SPECTRAL WEIGHTS

As was mentioned in the Introduction, the spectral weights of quasiparticles are felt by the spectroscopic methods. However, an analysis of their behavior in the Brillouin zone provides also a deeper understanding of nature of a material for the following reason. Being defined by Eq. (1), the spectral weight Z_{nk} indicates how much weight in many-electron systems can be ascribed to the *single-particle* excitations. According to Migdal's theorem [42], it determines the magnitude of the jump in Fermi distribution for the bands which cross Fermi surface. In a noninteractiing system, $Z_{nk} = 1$ whereas in the systems with interacting fermions $Z_{nk} < 1$ and, moreover, the stronger the interaction, the less is Z_{nk}. For this reason, it may be viewed also as an indicator of the interaction strength in k space. Since the states with s, p, and d origin experience different strength of the interaction due to their different degree of localization, it makes sense to perform an analysis of k dependence of the spectral weights together with the character coefficients C_{kn}, which show the partial contribution of s, p, and d states into formation of a band in question. Here, the coefficients C_{kn} are calculated by projecting the orbitals onto spherical harmonics using a quick projection scheme for PAW pseudopotentials [30]. Both Figs. 7 and 8 show that the spectral weights Z_{kn} within the G_0W_0 are strongly decreased.

As seen, the increase of Z_{kn} arises everywhere where an admixture of delocalized electron states is present. Indeed, one observes that near the X point of the Brillouin band it is the admixture of s and p electrons to d states for the band $T_{2g}^{(1)}$ of Fe_3Si causes the increase of the Z_{kn} [see Fig. 7(b)]. The picture for the empty bands is different: the s and p states of Si and d states of Fe are mixed in the center of the band, whereas the contribution of the d states is increased around boundary points X and L [Figs. 7(c) and 7(d)]. The quasiparticle energies of the excited states are lower than their Kohn-Sham counterparts. Again, the largest difference is observed in the those parts of the energy spectrum where the contributions from s and p states become significant.

As seen from Fig. 8, the spectral weights Z_{kn} of the quasiparticles in α-$FeSi_2$ also show a strongly nonmonotonous dependence on k. For example, the spectral weight $Z_{k,B_{1g}}$ of the B_{1g} band in the direction ΓX [second from top panel in Fig. 8(b)] shows sharp changes in the interval $0.55 < Z_{k,B_{1g}} < 0.8$. The lower part of Fig. 8(b) explains the reason: again, the closer to the X point the higher the contribution from the delocalized s electrons. Thus, the behavior of spectral weights indeed shows that the s electrons, being more delocalized, interact weaker than the d electrons. The conservation of the full spectral weight (it is equal to one as follows from the commutation relations for the orthonormal basis) gives birth to the question to be investigated: To which states is transferred the remaining weight $1 - Z$?

V. INFLUENCE OF SELF-CONSISTENCY ON THE QP BAND STRUCTURE

Since semilocalized d electrons are poorly described by GGA, it is expected that these errors are transferred to the one-shot G_0W_0. For this reason, we inspected the role played by the self-consistency in the formation of the QP band structure. As was mentioned in the Introduction, the self-energy in the present self-consistent GW calculation includes the vertex correction in the form $\delta\Gamma(1,2;3) = \delta(1,2) f_{xc}(2,3)$, suggested in Ref. [25]. The self-consistency is performed with respect to both QP energies and wave functions.

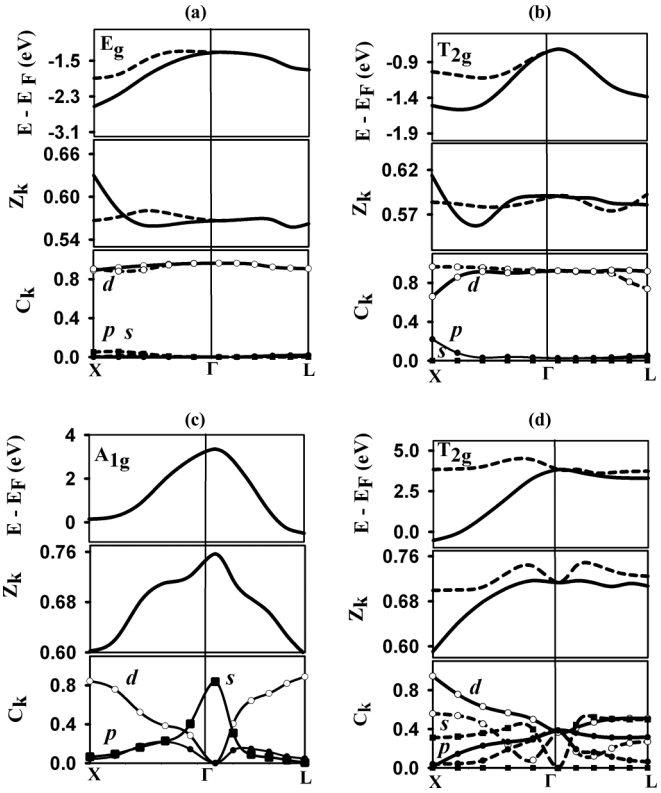

FIG. 7. Fe_3Si quasiparticle filled bands (top panels), their spectral weights Z_k (second from the top), and the s, p, d character coefficients C_k(bottom panels). The letters label different characters: d and p stand for the empty and filled circles, correspondingly, the black squares denote s character. The filled bands are shown in (a) and (b) panels, while (c) and (d) display the empty ones. The dashed and solid lines on (a) denote the nondegenerate bands E_g. The dashed and solid lines on (b) and (d) denote nondegenerate and double-degenerate bands T_{2g}.

The band structures of electrons in Fe_3Si calculated within GGA, G_0W_0, and scGW are shown on Fig. 9. While the difference between the bands generated by GGA and G_0W_0 calculations is quite weak, the scGWd-electron bands change their positions quite noticeably. First (down from Fermi level), three majority spin scGW bands formed by d electrons of both Fe atoms are shifted down from Fermi energy by (0.15–0.2) eV. Similar shifts experience two minority-spin filled bands formed by T_{2g} electrons of both $Fe^{(1)}$ and $Fe^{(2)}$: their shape is not changed, however, they are shifted upward, towards the Fermi level; the first band is shifted by (0.15–0.2) eV.

An interesting change of the band structure arises near the X point for the minority-spin bands: if the GGA calculation predicts a small pocket on the Fermi surface (Fig. 9, right column in the bottom panel), G_0W_0 removes it, pushing these

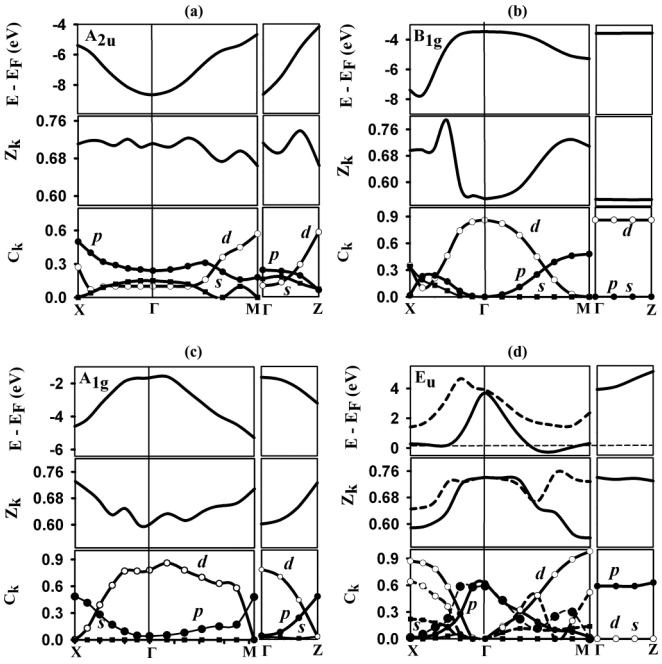

FIG. 8. The α-$FeSi_2$ bands. The notations are the same as in Fig. 7, but the filled bands are imaged in panels (a)–(c), while the empty one is shown in (d).

states slightly above (0.1 eV) Fermi energy, while scGW lifts them farther by ∼0.4 eV upward. At the same time, the pocket for majority-spin states within scGW (Fig. 9, left column in the bottom panel) even increases its size compared to GGA. Thus, scGW predicts different *topology* of the Fermi surfaces for majority- and minority-spin states compared to GGA. This allows to expect, thus, that this difference can be observed, e.g., in the de Haas–van Alphen effect measurements. Besides, two almost flat scGW bands of E_g symmetry move apart. This tendency has been observed already in G_0W_0 calculation, but there it was quite weak. Thus, one can conclude that self-consistency with f_{XC} correction shifts all, localized and delocalized, d-electron states. The observed fact that scGW changes the spectral weights negligibly, by 2%–5% in spite of noticeable changes in scGW band structure compared to G_0W_0, says that the energy dependence of the self-energy remains almost the same $[\partial\Sigma(\Gamma)/\partial E \approx 0]$.

Contrary to the situation with Fe_3Si, scGW calculation on α-$FeSi_2$ does not reveal qualitative difference in the band dispersion with the one in the one-shot approximation G_0W_0 (see Fig. 10). A general feature of scGW approximation for both compounds is the tendency of bands to converge to the GGA bands. Especially, this tendency manifests itself in α-$FeSi_2$. Notice that the scGW lifts upward all bands, and the bands of excited states now are higher than those obtained in GGA. Since the spectral weights for this compound remain almost the same too, i.e., $Z_k^{G_0W_0} \approx Z_k^{scGW}$, we can conclude that the used vertex-corrected part of the self-energy just adds almost energy-independent potential into the self-energy.

It is also interesting that influence of scGW is weaker in the energy region in vicinity of Fermi energy and stronger apart from it (for both excited and filled bands). Similar effect has been observed in Ref. [43]. There are, however,

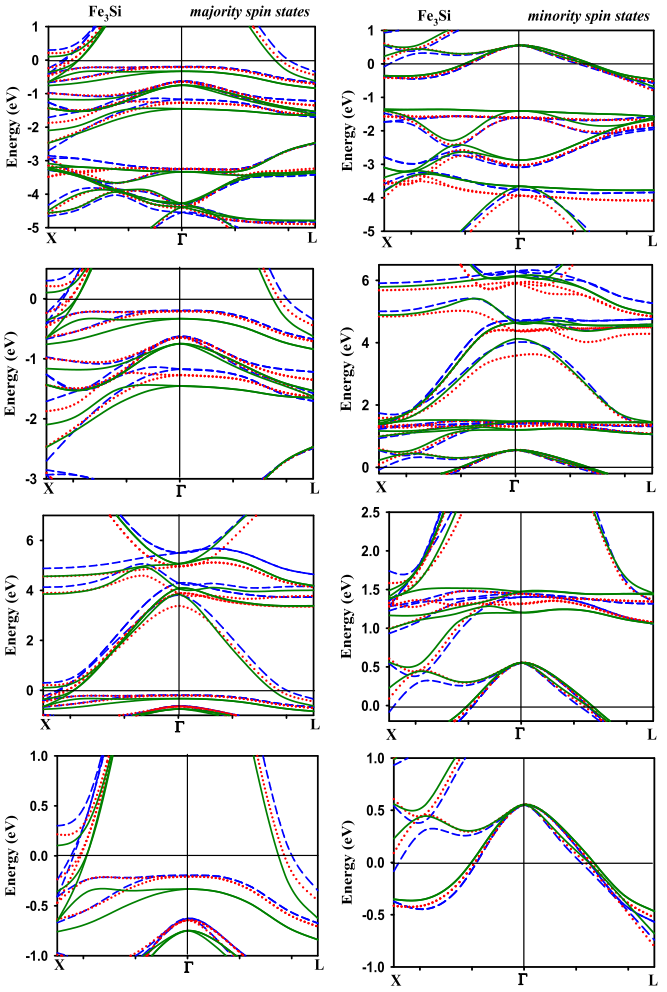

FIG. 9. (Color online) Comparison of Fe_3Si band structures in some of symmetrical directions: GGA (dashed lines), G_0W_0 (dotted lines), and scGW (solid lines). From top to bottom: the filled bands, the bands of excited states, and the energy region in the vicinity of the Fermi level.

qualitative differences between the results if scGW applied to semiconductor GaAs and to metal α-$FeSi_2$. In the former case, G_0W_0 and scGW move the bands downward in energy while in α-$FeAs_2$ these approximations act in opposite direction. Such unambiguous influence scGW on the bands in Fe_3Si is not observed.

VI. OPTICAL PROPERTIES OF Fe_3Si

Although the optical properties have been calculated in all three approximations for both iron silicides, experimentally only the samples of Fe_3Si thick films have been grown and investigated. For this reason, we present here the theoretical results only for Fe_3Si.

A. Fe_3Si experiment

The Fe_3Si film was grown on 1° miscut vicinal n-Si(111) wafer with resistivity of 5–10 Ω cm at 160 °C by the method of thermal evaporation in ultrahigh vacuum condition (UHV) in modernized molecular-beam epitaxy (MBE)

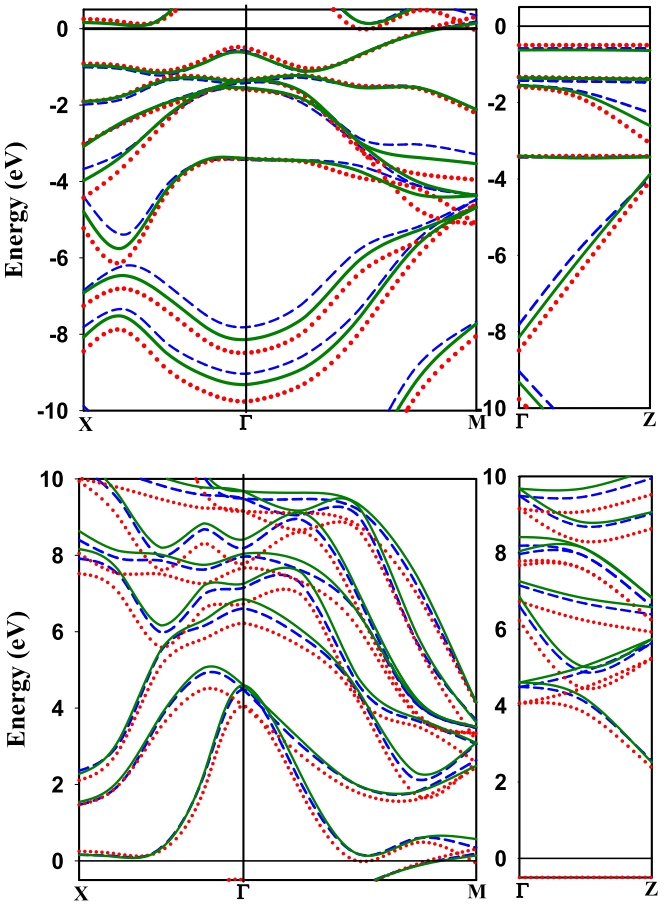

FIG. 10. (Color online) Comparison of α-$FeSi_2$ band structures in some of symmetrical directions: GGA (dashed lines), G_0W_0 (dotted lines), and scGW (solid lines). From top to bottom: the filled bands, the bands of excited states, and the energy region in the vicinity of the Fermi level.

chamber Angara [44], equipped with reflection high-energy electron diffraction (RHEED). Prior to growth, Si wafer was chemically cleaned by a technique described in Ref. [5]. In UHV (base pressure 6.5×10^{-8} Pa), a Si wafer was exposed to gradual thermal treatment for 3 h to 650 °C at rate of 4 °C/min. In order to obtain an atomically clean silicon surface, the wafer was flashed at 850 °C–900 °C until well-ordered (7×7) reconstruction appeared in RHEED pattern. After the sample was cooled down to 160 °C, Fe and Si were deposited simultaneously with growth rates of 0.772 and 0.44 nm/min. The as-grown RHEED pattern clearly displays symmetrical streaks, which implies a good two-dimensional growth of the Fe_3Si film on Si(111) surface. X-ray diffraction measurements of the Fe_3Si/Si(111) were performed on a PANalytical X'Pert PRO diffractometer equipped with a solid-state detector PIXcel on Co Ka radiation. The in-plane epitaxial orientation was analyzed using the asymmetrical ϕ scans of reflections 224 from the Fe_3Si film and Si substrate (Fig. 11), which revealed the following orientation relations: $Fe_3Si(111)[1-21]||Si(111)[11-2]$. For the crystal-structure analysis, a series of characteristic reflections 111, 222, 224, and 440 from the Fe_3Si film were measured choosing respective tilt angles and ϕ orientations of the sample (Fig. 12). To

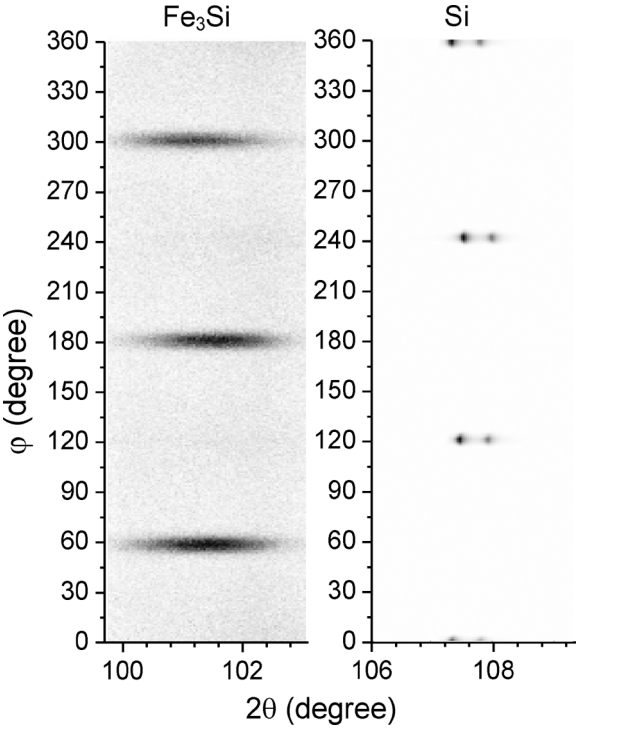

FIG. 11. Two-dimensional images for ϕ scans of reflections 224 from Fe_3Si film and Si substrate.

reduce the 111 reflection from the Si substrate, an additional tilt of 1° was applied. The cubic $(Fm3m)$ lattice parameter $a = 5.6650(2)$ Å and the occupancies of Fe and Si positions in the crystal structure (Table II) were determined from the XRD pattern by the derivative difference minimization method [45].

The dielectric permittivity has been calculated via variable angle spectroscopic ellipsometry using the method described in detail in Ref. [46]. In the calculations, we used the optical model involving a homogeneous isotropic film with unknown thickness and dielectric permittivity on an isotropic Si substrate with known optical characteristics. The measurements were performed at $T = 296$ K using the Ellips-1891 high-speed spectral ellipsometer. As opposed to the work [46], all

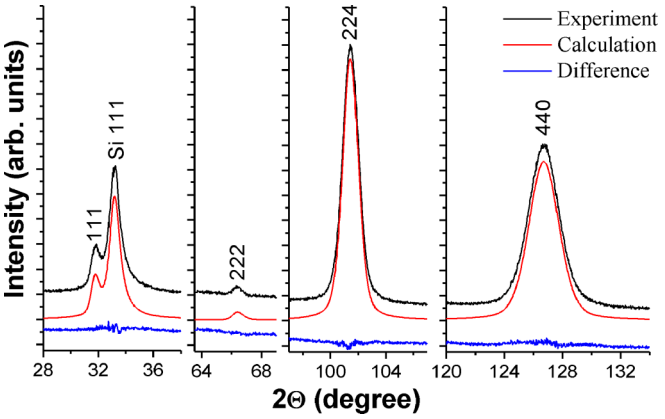

FIG. 12. (Color online) Observed, calculated, and difference XRD patterns for four characteristic diffraction peaks of Fe_3Si after crystal-structure refinement.

TABLE II. Occupancies of Fe and Si positions in Fe_3Si crystal structure.

Wyckoff position	8*c* ($Fe^{(1)}$)	4*a* ($Fe^{(2)}$)	4*b* (Si)
Fe	0.95(1)	0.70(1)	0.40(1)
Si	0.05(1)	0.30(1)	0.60(1)

combinations of ellipsometric data measured across the whole wavelength range at six different angles were used to calculate average parameter of the film thickness, which was revealed to be 501.4 nm. Such optical characteristics as complex refractive index, reflectivity, absorption coefficient, and electron energy losses have been calculated from the dielectric permittivity using formulas given in corresponding figure captions.

B. Comparison of theoretical and experimental results

As mentioned in Sec. II, we obtained real and imaginary parts of permittivity (ϵ' and ϵ'') from our *ab initio* calculations and other optical characteristics are calculated from the permittivity using formulas in the captions to Figs. 15–19. The calculated optical characteristics show only qualitative agreement with experimental ones. In comparison to the sharp features observed on theoretical curves, the experimental ones are quite smooth. There are several mechanisms which may contribute to the measurements on real samples, which wash out the sharp peaks, found theoretically. There can be dislocations and stacking faults arising in the course of the island coalescence, the disorder in the positions of Si and Fe atoms (see Table II). In addition, a contribution to the tailing of the spectra can come from the thermal processes. None of these mechanisms are taken into account by any of the approximations used, GGA, G_0W_0A, and GWA. Nevertheless, we did not introduce a phenomenological smoothing into theoretical curves, hoping that future experiments (particularly, at low temperature), possibly, will reveal more detailed structure. For this reason, at present we are able to perform only qualitative comparison of experiment and theory.

Let us start with permittivity (Figs. 13 and 14). As seen from Fig. 13, theoretical curves describe the experiment well in the interval of frequencies $\omega \in (2.2,5)$ eV. In the interval $\omega \in (1.2,2.2)$ eV, both theoretical curves are lower than the experimental one. However, the position of the peak $\omega^0_{G_0W_0} \simeq$ 1.7 eV obtained within G_0W_0 is shifted by scGW to the right position $\omega^0_{scGW} \simeq 1.25$ eV.

The main clearly observed feature in the imaginary part of the experimental dielectric permittivity (Fig. 14) is a wide peak at ~1.5 eV. The approximation G_0W_0 generates the peak at ~1.8 eV, while the scGW one shifts this peak towards experimentally observed position, ~1.5 eV. The analysis shows that the main contribution to formation of this peak comes from the minority-spin states. Indeed, there are two close to the Fermi surface filled spin-down bands in the direction ΓX (flat band at the −1.2 eV and the partially filled band at the −0.3 eV) and partially filled band near the *L* point. The transitions from these bands to the almost flat in the same *k*-direction empty band matches well to the photon energy ~1.5 eV. Since part of considered bands are flat, the phase

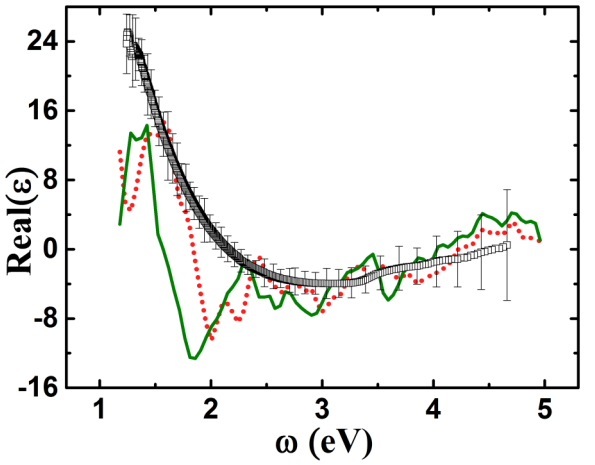

FIG. 13. (Color online) Real part of permittivity $\epsilon' = \mathrm{Re}(\epsilon)$ of Fe_3Si. Squares denote experimental data, (red) dashed line presents result of G_0W_0, (green) solid lines displays the result of the scGW calculation.

volume contributing to permittivity is large, which results in the peak in question.

The shift of the peak in the scGW calculation compared to the G_0W_0 one is due to shift of the filled scGW T_{2g} minority-spin band up by 0.3 eV from the G_0W_0 value. One can expect also that the greater value of disorder occurring between $Fe^{(2)}$ and Si sites in the Fe_3Si film discussed above (see Table II) results in a peak broadening at photon energies ~2.5 and ~3.5 eV while a two times smaller disorder between $Fe^{(1)}$ and Si sites is less destructive.

The behavior of the refractive index (Fig. 15) is similar to the one of the real part of permittivity: scGW shifts main peak in right direction compared to the one-shot approximation G_0W_0. Surprisingly, however, this is not so for the extinction coefficient (Fig. 16): the G_0W_0 describes the position of the peak at $\omega \simeq 2$ eV better than scGW. The dip at $\omega \simeq 4.4$ eV, predicted by both G_0W_0 and scGW, possibly, is smeared

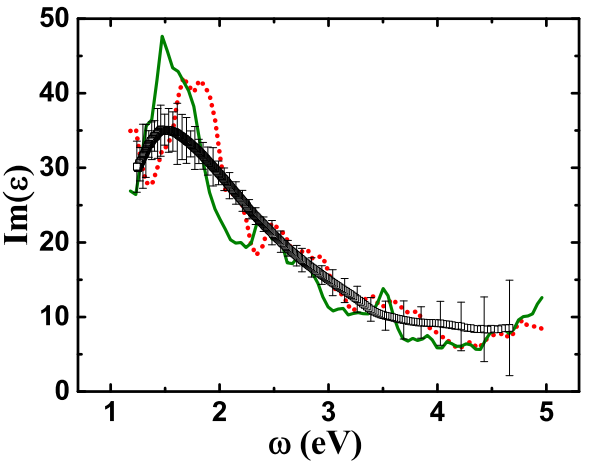

FIG. 14. (Color online) Imaginary part of permittivity $\epsilon'' = \mathrm{Im}(\epsilon)$ of Fe_3Si. Squares denote experimental data, (red) dashed line presents result of G_0W_0, (green) solid lines displays the result of the scGW calculation.

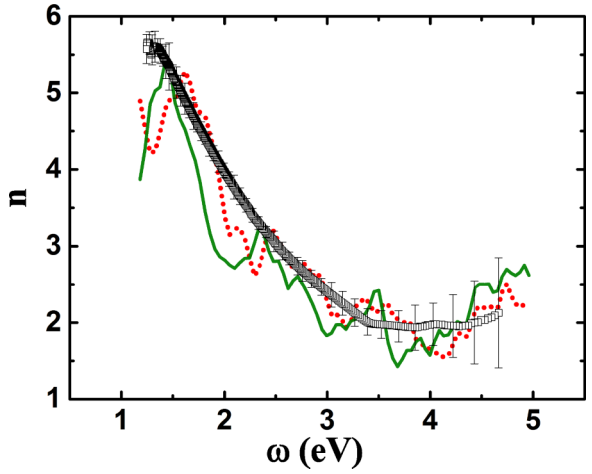

FIG. 15. (Color online) Refractive index $n = \{[|\epsilon| + \mathrm{Re}(\epsilon)]/2\}^{1/2}$ of Fe_3Si. Squares denote experimental data, (red) dashed line presents result of G_0W_0, (green) solid lines displays the result of the scGW calculation.

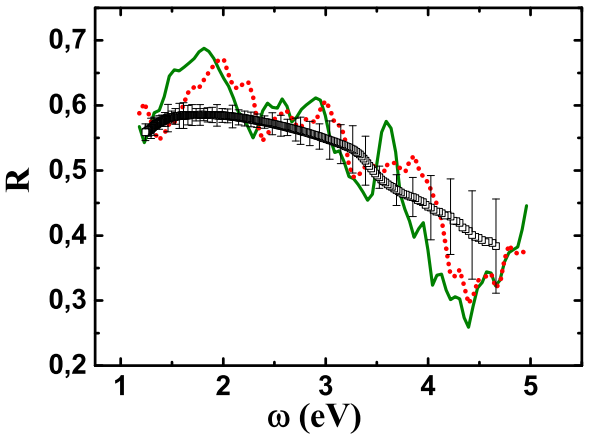

FIG. 17. (Color online) Reflectivity $R = \{[(n-1)^2 + k^2]/[(n+1)^2 + k^2]\}$ of Fe_3Si. Squares denote experimental data, (red) dashed line presents result of G_0W_0, (green) solid lines display the result of the scGW calculation.

out by large errors inherent to the experiment in this region of frequencies. The last statement is valid in this region of frequencies also for the reflectivity (Fig. 17), electron energy loss function (Fig. 18), and absorption coefficient (Fig. 19).

Thus, the low-energy peaks, predicted by both G_0W_0 and scGW, in real part of permittivity, reflectivity, extinction, and absorption coefficients, are not seen in experimental curves.

VII. DISCUSSION AND CONCLUSIONS

The comparison of the band structures obtained in the *ab initio* calculations within the VASP for Fe_3Si and α-$FeSi_2$ in GGA and GW shows that in general the bands' shape is similar. The difference between GGA and GW bands becomes more pronounced in those parts of the Brillouin zone where the delocalized states give noticeable contribution into quasiparticle energies. This observation is somewhat unexpected since both approximations are designed for description of well-delocalized (Fermi-liquid-like) electrons. There are at least two sources which can contribute to this difference. First is the fact that the standard GGA is not free from the self-interaction while GW takes into account Fermi statistics by construction. The second source is that GGA and GW are quite different approximations, as was discussed in the Introduction. Particularly, it is worth noting that even if the exchange-correlation potential v_{XC} was found from the Sham-Slüter equation for some approximation of the self-energy $\Sigma(\omega)$, it would not mean that the perturbation theory with respect to the difference $v_{XC} - \Sigma(\omega)$, used in the widely used one-short approximation G_0W_0, is good. The reason is that the Dyson's equation for the Green's function should be fulfilled at each energy point, while the Sham-Slüter equation is written for integrals over all energies. From this point of view, the origin of such a close similarity of the Kohn-Sham bands with the energies of quasiparticle excitations remains unclear.

The observed decrease of the spectral weights Z_{kn} of the quasiparticle bands E_{kn} arises in any approximation with

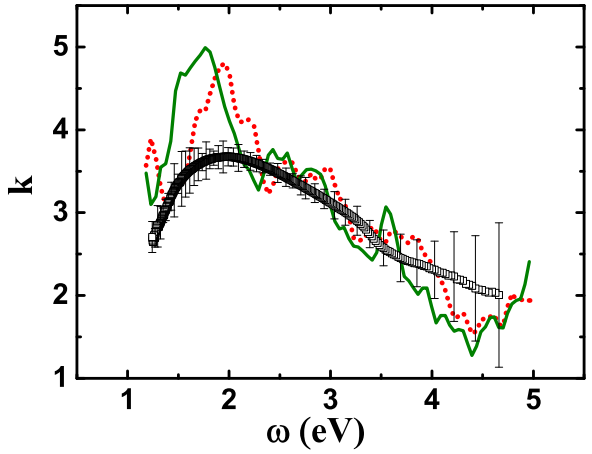

FIG. 16. (Color online) Extinction coefficient $k = \{[|\epsilon| - \mathrm{Re}(\epsilon)]/2\}^{1/2}$ of Fe_3Si. Squares denote experimental data, (red) dashed line presents result of G_0W_0, (green) solid lines display the result of the scGW calculation.

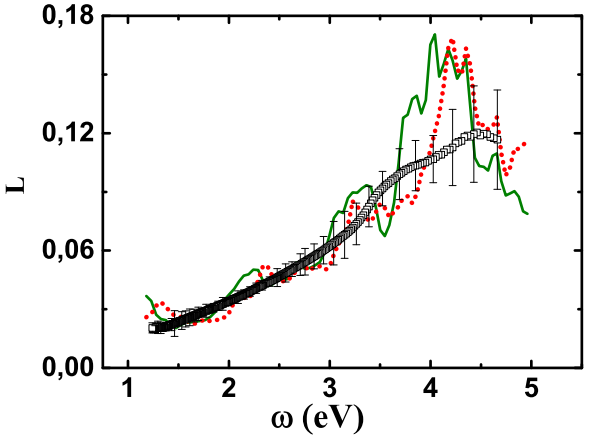

FIG. 18. (Color online) Electron energy loss function $L = \mathrm{Im}(\epsilon)/|\epsilon|^2$ of Fe_3Si. Squares denote experimental data, (red) dashed line presents result of G_0W_0, (green) solid lines display the result of the scGW calculation.

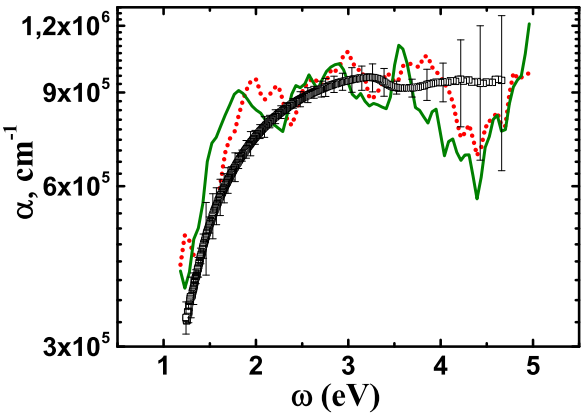

FIG. 19. (Color online) Absorption coefficient $\alpha = 2\omega k/c$ of Fe_3Si. Squares denote experimental data, (red) dashed line presents result of G_0W_0, (green) solid lines display the result of the scGW calculation.

energy-dependent self-energy Σ since $d\Sigma/dE < 1$ [42]. The GW calculations produced this decrease almost by a half even for the systems with well-delocalized electrons at the densities of real metallic systems. This fact is well known from the calculations for homogeneous electron gas (see detailed discussion in the Mahan's book [47]). In order to check this conclusion, we performed the GW calculations for Na metal. The obtained spectral weights are found in the interval 0.5–0.6 as expected for such density of the gas. One can assume that the GW shifts the remaining part of the weight to the incoherent part of excitations.

Both GGA and GW band structures and, correspondingly, the density of electron states, show that the d electrons of those Fe atoms which have Si nearest neighbors, namely, $Fe^{(2)}$ atoms for Fe_3Si and all Fe atoms in α-$FeSi_2$, are more delocalized than the d electrons of $Fe^{(1)}$ atoms in Fe_3Si, which are surrounded only by the other Fe atoms. The partial density of states of $Fe^{(1)}$ d electrons with E_g and T_{2g} symmetry in the Γ point has well-expressed peaks, the positions of which could be ascribed to a splitting in the crystal field. However, this splitting does not correspond to the standard picture of the quasiatomic levels $\varepsilon^0_{T_{2g},\sigma} d^\dagger_{t\sigma} d_{t\sigma} + \varepsilon^0_{E_g,\sigma} d^\dagger_{e\sigma} d_{e\sigma}$, from which the bands are formed; the interactions renormalize these "levels" $\varepsilon^0_{T_{2g},\sigma} \to \varepsilon_{T_{2g},\sigma}$ in such a way that their sequence becomes $\varepsilon_{T_{2g},\uparrow} < \varepsilon_{T_{2g},\downarrow}$, $\varepsilon_{E_g,\uparrow} < \varepsilon_{T_{2g},\uparrow}$.

The reduction of the spectral weight predicted by our GW calculation may be verified by the ARPES experiments. If the DFT-GGA band structure was correct and could be interpreted as a QP spectrum, the momentum distribution curve would reveal the uniform distribution of the spectral weight along the Fermi surface. Thus, the ARPES experiments on iron silicides would be of great help in further understanding of these compounds and, possibly, could motivate more advanced theoretical approach to the problem.

The optical experiments on Fe_3Si thick films performed in this work allowed us to obtain real $\mathrm{Re}(\epsilon)$ and imaginary $\mathrm{Im}(\epsilon)$ parts of the permittivity ϵ and, correspondingly, the refractive index n, reflectivity R, electron energy loss function L, extinction k, and absorption α coefficients. Our G_0W_0 and scGW calculations show that $\mathrm{Re}(\epsilon)$, $\mathrm{Im}(\epsilon)$, R, k, α display low-energy peaks at energies $\sim$(1.5–1.8) eV. The detailed structure of these peaks is not seen in experiment, however, its position in $\mathrm{Re}(\epsilon)$ and $\mathrm{Im}(\epsilon)$ calculated within scGWA is closer to experiment than the G_0W_0A one. At the same time, these peaks are completely washed out in experimental R, k, and α. As has been discussed in the beginning of Sec. VI B, quasiparticle band structure suggests that these peaks originate from particle-hole transitions between the flat-filled and empty bands.

One can assume that a possible reason for the observed discrepancy might be the spin-orbit coupling which is not taken into account in our calculations. However, as it is known from the experiment [48], the orbital moment in the stoichiometric Fe_3Si is quite small, only $0.051\mu_B$. Our calculations within the GGA give the orbital moment in Fe_3Si $0.046\mu_B$ on $Fe^{(1)}$ and $0.02\mu_B$ on $Fe^{(2)}$ (average orbital moment calculated in Ref. [48] is $0.029\mu_B$), whereas in α-$FeSi_2$ it is $0.00005\mu_B$. Thus, the spin-orbit interaction is too small to be able to remove the discrepancy.

The clear physical origin of these peaks, derived from *ab initio* calculations, raises the following: either the G_0W_0 and the scGW approximations are not good enough, or further experiments are needed on better quality samples and at low temperature. This also can be solved in ARPES experiments: if the flat bands will be found and, therefore, the approximation used correctly reflects the quasiparticle properties, the reason for discrepancy with results of the optical experiments should be ascribed to insufficient accuracy of experiment. And, *vice versa*, if ARPES will not reveal these flat bands, a better approximation for calculation of quasiparticle properties should be developed.

One more difference between the GGA and GW results is worth mentioning. Although the Fermi surface was not calculated in this work, it is clear from the comparison of GGA and GW band structures that the GW generates different Fermi-surface topology for the majority- and minority-spin states: the small pocket existing near the X point in GGA disappears in in GW calculations. In this respect, the measurements of the de Haas–van Alphen effect on Fe_3Si would be of help.

The technological impact of this paper is straightforward. The possibility of single-crystalline MBE films of Fe silicides on the Si substrate growth [3–5] opens the way to (ferromagnetic metal)/(nonmagnetic semiconductor) heterostructures with silicide layers,where Fe_3Si layers should work as spin injectors. The example of MBE structure Fe_3Si/Ge/Fe_3Si/Si has been demonstrated in the paper [49]. The *in situ* spectral magnetoellipsometry allows to control the optical parameters (real and imaginary parts of the diagonal component of dielectric permittivity tensor) and magnetic properties (off-diagonal components) [50], that are directly related to the quality of silicide nanolayers. To get the material parameters from the magnetoellipsometry measurements, the theoretical knowledge of the spectral dependence of the dielectric permittivity is necessary.

ACKNOWLEDGMENTS

The theoretical part of this work was supported by Russian Fund of Basic Research, Grant No. 14002-00186 and the President of Russia Grants No. 2886.2014.2 and No. 924.2014.2

for support of Leading Scientific School. The calculations were performed with the computer resources of NRC "Kurchatov Institute" (ui2.computing.kiae.ru). The experimental work was supported by Russian Fund of Basic Research, Grant No. 13-02-01265. I.S. thanks A. Ruban for useful discussion.

[1] S. A. Wolf, D. D. Awschalom, R. A. Buhrman, J. M. Daughton, S. von Molnar, M. L. Roukes, A. Y. Chtchelkanova, and D. M. Treger, Science **294**, 1488 (2001).

[2] Guixin Cao, D. J. Singh, X.-G. Zhang, German Samolyuk, Liang Qiao, Chad Parish, Ke Jin, Yanwen Zhang, Hangwen Guo, Siwei Tang, Wenbin Wang, Jieyu Yi, Claudia Cantoni, Wolter Siemons, E. A. Payzant, Michael Biegalski, T. Z. Ward, David Mandrus, G. M. Stocks, and Zheng Gai, Phys. Rev. Lett. **114**, 147202 (2015).

[3] K. Hamaya, K. Ueda, Y. Kishi, Y. Ando, T. Sadoh, and M. Miyao, Appl. Phys. Lett. **93**, 132117 (2008).

[4] R. Nakane, M. Tanaka, and S. Sugahara, Appl. Phys. Lett. **89**, 192503 (2006).

[5] I. A. Yakovlev, S. N. Varnakov, B. A. Belyaev, S. N. Zharkov, M. S. Molokeev, I. A. Tarasov, and S. G. Ovchinnikov, JETP Lett. **99**, 527 (2014).

[6] C. J. Umrigar, A. Savin, and Xavier Gonze, in *Electronic Density Functional Theory: Recent Progress and New Directions*, edited by J. F. Dobson, G. Vignale, and M. P. Das (Plenum, New York, 1997), pp. 1–10.

[7] E. Wimmer, H. Krakauer, M. Weinert, and A. J. Freeman, Phys. Rev. B **24**, 864 (1981).

[8] J. Kudrnovsky, N. E. Christensen, and O. K. Andersen, Phys. Rev. B **43**, 5924 (1991).

[9] H. J. F. Jansen and A. J. Freeman, Phys. Rev. B **30**, 561 (1984).

[10] H. L. Skriver, *The LMTO Method* (Springer, New York, 1984).

[11] O. K. Andersen, Phys. Rev. B **12**, 3060 (1975).

[12] Stefan Hüfner, *Photoelectron Spectroscopy, Principles and Applications*, 2nd ed., Springer Series in Solid-State Sciences, Vol. 82 (Springer, Berlin, 1996).

[13] H. Ueba and B. Gumhalter, Prog. Surf. Sci. **82**, 193 (2007).

[14] F. Aryasitiawan and O. Gunnarsson, Rep. Prog. Phys. **61**, 237 (1998); W. G. Aulbur, L. Jönsson, and J. W. Wilkins, Solid State Phys. **54**, 1 (1999).

[15] John M. Wills, Mebarek Alouani, Per Andersson, Anna Delin, Olle Eriksson, and Oleksiy Grechnyev, in *Full-Potential Electronic Structure Method Energy and Force Calculations with Density Functional and Dynamical Mean Field Theory*, Springer Series in Solid-State Sciences Series, Vol. 167, edited by M. Cardona, P. Fulde, K. von Klitzing, R. Merlin, H.-J. Queisser, and H. Störmer (Springer, Berlin, 2010), p.151.

[16] V. I. Anisimov, I. V. Solovyev, M. A. Korotin, M. T. Czyźyk, and G. A. Sawatzky, Phys. Rev. B **48**, 16929 (1993); M. T. Czyźyk and G. A. Sawatzky, *ibid.* **49**, 14211 (1994); A. I. Lichtenstein, M. I. Katsnelson, and G. Kotliar, Phys. Rev. Lett. **87**, 067205 (2001); M. I. Katsnelson and A. I. Lichtenstein, Eur. Phys. J. B. **30**, 9 (2002); J. Kuneš, V. I. Anisimov, A. V. Lukoyanov, and D. Vollhardt, Phys. Rev. B **75**, 165115 (2007); B. Amadon, F. Lechermann, A. Georges, F. Jollet, T. O. Wehling, and A. I. Lichtenstein, *ibid.* **77**, 205112 (2008); I. Leonov, A. I. Poteryaev, V. I. Anisimov, and D. Vollhardt, Phys. Rev. Lett. **106**, 106405 (2011); M. Karolak, G. Ulm, T. Wehling, V. Mazurenko, A. Poteryaev, and A. Lichtenstein, J. Electron Spectrosc. Relat. Phenom. **181**, 11 (2010); I. A. Nekrasov, N. S. Pavlov, M. V. Sadovskii, JETP Lett. **95**, 581 (2012); JETP **116**, 620 (2013).

[17] M. Shishkin and G. Kresse, Phys. Rev. B **74**, 035101 (2006); F. Fuchs, J. Furthmüller, F. Bechstedt, M. Shishkin, and G. Kresse, *ibid.* **76**, 115109 (2007).

[18] Giovanni Onida, Lucia Reining, and Angel Rubio, Rev. Mod. Phys. **74**, 601 (2002).

[19] F. Caruso, P. Rinke, X. Ren, M. Scheffler, and A. Rubio, Phys. Rev. B **86**, 081102 (2012); N. Marom, F. Caruso, X. Ren, O. T. Hofmann, T. Körzdörfer, J. R. Chelikowsky, A. Rubio, M. Scheffler, and P. Rinke, *ibid.* **86**, 245127 (2012).

[20] Adrian Stan, Nils Erik Dahlen, and Robert van Leeuwen, J. Chem. Phys. **130**, 114105 (2009).

[21] C. Rostgaard, K. W. Jacobsen, and K. S. Thygesen, Phys. Rev. B **81**, 085103 (2010).

[22] M. Shishkin, M. Marsman, and G. Kresse, Phys. Rev. Lett. **99**, 246403 (2007).

[23] Andreas Gruneis, Georg Kresse, Yoyo Hinuma, and Fumiyasu Oba, Phys. Rev. Lett. **112**, 096401 (2014).

[24] Some of the problems where both particle-particle and particle-hole channels of scattering give comparable contributions to the vertex (parquet problems). V. V. Sudakov, Dokl. Akad. Nauk **111**, 338 (1956) [Sov. Phys. Dokl., **1**, 662 (1957)]; A. A. Abrikosov, Physics **2**, 21 (1965); B. Roulet, P. J. Garovet, and Noziéres, Phys. Rev. **178**, 1072 (1969); A. N. Podmarkov and I. S. Sandalov, Zh. Eksp. Teor. Fiz. **95**, 2235 (1989) [Sov. Phys.-JETP **68**, 1291 (1989)]; V. Yu. Irkhin, A. A. Katanin, and M. I. Katsnelson, Phys. Rev. B **64**, 165107 (2001).

[25] P. Romaniello, S. Guyot, and L. Reining, J. Chem. Phys. **131**, 154111 (2009); Fabien Bruneval, Francesco Sottile, Valerio Olevano, Rodolfo Del Sole, and Lucia Reining, Phys. Rev. Lett. **94**, 186402 (2005).

[26] Runge-Gross theorem of TDDFT [27] have been used Ref. [25] in order to express the three-point vertex $\Gamma(1,2;3) = \delta\Sigma(1,2)/\delta V(3)$ in terms of functional derivative with respect to electron density $\delta\Sigma(1,2)/\delta V(3) = [\delta\Sigma(1,2)/\delta\rho(4)][\delta\rho(4)/\delta V(3)]$. Adding and subtracting the term $\delta f_{\rm xc}^{\rm eff} P$ to the vertex $\Gamma = \delta f_{\rm xc}^{\rm eff} P + (\Gamma - \delta f_{\rm xc}^{\rm eff} P) = \delta f_{\rm xc}^{\rm eff} P + \Delta\Gamma$ they divided the into three terms $\Gamma(1,2;3) = \delta(1,2)\delta(2,3) + \delta(1,2) f_{\rm xc}^{\rm eff}(1,4) P(4,3) + \Delta\Gamma(1,2;3)$ with $f_{\rm xc}^{\rm eff}(1,4) = -i P_0^{-1}(1,6) G(65) G(76) \delta\Sigma(5,7)/\delta\rho(4)$, where $P_0(12) = -i G(12) G(21)$ and gave the arguments when $\Delta\Gamma$ can be neglected.

[27] E. Runge and E. K. U. Gross, Phys. Rev. Lett. **52**, 997 (1984).

[28] Andrew J. Morris, Martin Stankovski, Kris T. Delaney, Patrick Rinke, P. Garcia-González, and R. W. Godby, Phys. Rev. B **76**, 155106 (2007).

[29] G. Kresse and J. Furthmüller, Comput. Mat. Sci. **6**, 15 (1996); Phys. Rev. B **54**, 11169 (1996).

[30] P. E. Blöchl, Phys. Rev. B **50**, 17953 (1994); G. Kresse and D. Joubert, *ibid.* **59**, 1758 (1999).

[31] J. P. Perdew, K. Burke, and M. Ernzerhof, Phys. Rev. Lett. **77**, 3865 (1996); **78**, 1396 (1997).
[32] M. Gajdos, K. Hummer, G. Kresse, J. Furthmuller, and F. Bechstedt, Phys. Rev. B **73**, 045112 (2006).
[33] H. J. Monkhorst and J. D. Pack, Phys. Rev. B **13**, 5188 (1976).
[34] P. Villars and L. D. Calvert, *Pearson's Handbook of Crystallographic Data for Intermetallic Phases* (American Society for Metals, Materials Park, OH, 1985).
[35] S. Eisebitt, J.-E. Rubensson, M. Nicodemus, T. Boske, S. Blugel, W. Eberhardt, K. Radermacher, S. Mantl, and G. Bihlmayer, Phys. Rev. B **50**, 18330 (1994).
[36] N. E. Christensen, J. Kudrnovský, and C. O. Rodriguez, Int. J. Mater. Sci. Simul. **1**, 1 (2007).
[37] W. A. Hines, A. H. Menotti, J. I. Budnick, T. J. Burch, T. Litrenta, V. Niculescu, and K. Raj, Phys. Rev. B **13**, 4060 (1976).
[38] E. G. Moroni, W. Wolf, J. Hafner, and R. Podloucky, Phys. Rev. B **59**, 12860 (1999).
[39] E. J. D. Carba and R. L. Jacobs, J. Phys. F: Met. Phys. **16**, 1485 (1986).
[40] R. Girlanda, E. Piparo, and A. Balzarotti, J. Appl. Phys. **76**, 2837 (1994).
[41] J. van Ek, P. E. A. Turchi, and P. A. Sterne, Phys. Rev. B **54**, 7897 (1996).
[42] A. B. Migdal, ZhETF **32**, 399 (1957) [Sov. Phys. JETP **5**, 333 (1957)].
[43] Sergey V. Faleev, Mark van Schilfgaarde, and Takao Kotani, Phys. Rev. Lett. **93**, 126406 (2004).
[44] S. N. Varnakov, A. A. Lepeshev, S. G. Ovchinnikov, A. S. Parshin, M. M. Korshunov, and P. Nevoral, Instrum. Exp. Tech. **47**, 839 (2004).
[45] L. A. Solovyov, J. Appl. Crystallogr. **37**, 743 (2004).
[46] F. K. Urban III, D. Barton, and T. Tiwald, Thin Solid Films **518**, 1411 (2009).
[47] G. D. Mahan, *Many-Particle Physics*, 2nd ed. (Plenum, New York, 1993), p. 482 (the spectral weights for different densities of the homogeneous gas are given in the Table 5.6).
[48] K. Zakeri, S. J. Hashemifar, J. Lindner, I. Barsukov, R. Meckenstock, P. Kratzer, Z. Frait, and M. Farle, Phys. Rev. B **77**, 104430 (2008).
[49] Shinya Yamada, Masanobu Miyao, and Kohei Hamaya, in *7th International Silicon-Germanium Technology and Device Meeting (ISTDM)* (IEEE, Piscataway, NJ, 2014).
[50] S. A. Lyashchenko, Z. I. Popov, S. N. Varnakov, E. A. Popov, M. S. Molokeev, I. A. Yakovlev, A. A. Kuzubov, S. G. Ovchinnikov, T. S. Shamirzaev, A. V. Latyshev, and A. A. Saranin, JETP **120**, 886 (2015).